



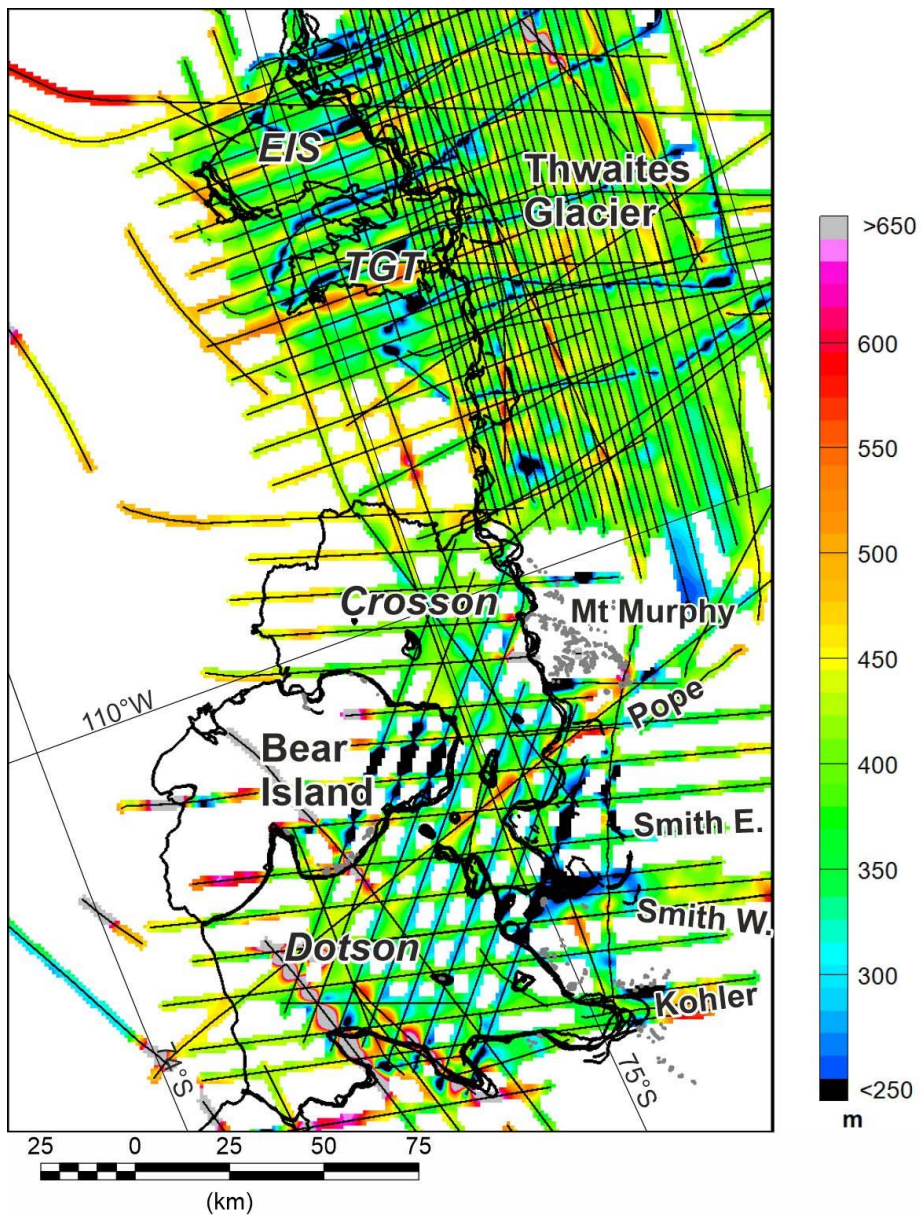
Supplement of

New gravity-derived bathymetry for the Thwaites, Crosson, and Dotson ice shelves revealing two ice shelf populations

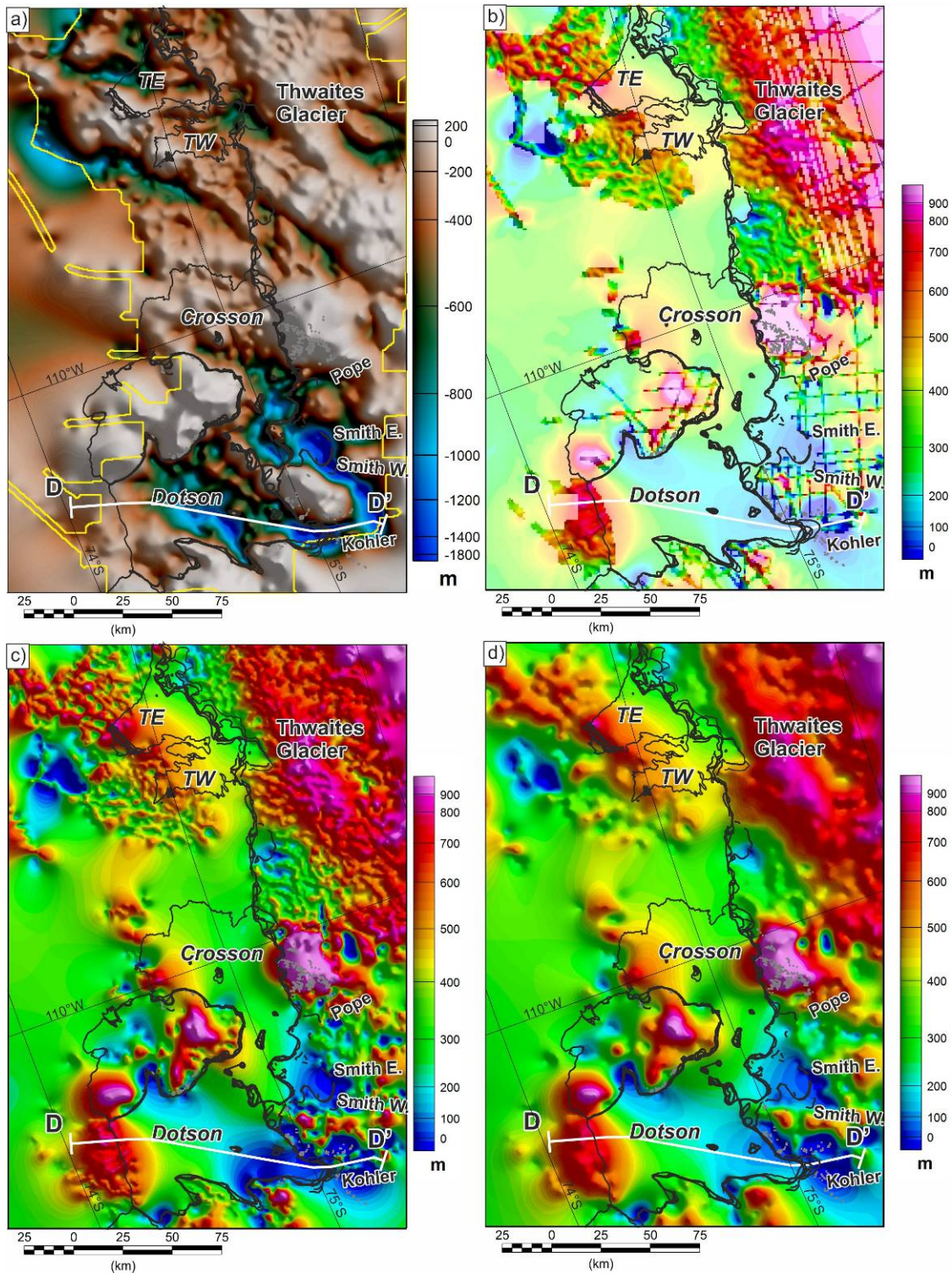
Tom A. Jordan et al.

Correspondence to: Tom A. Jordan (tomj@bas.ac.uk)

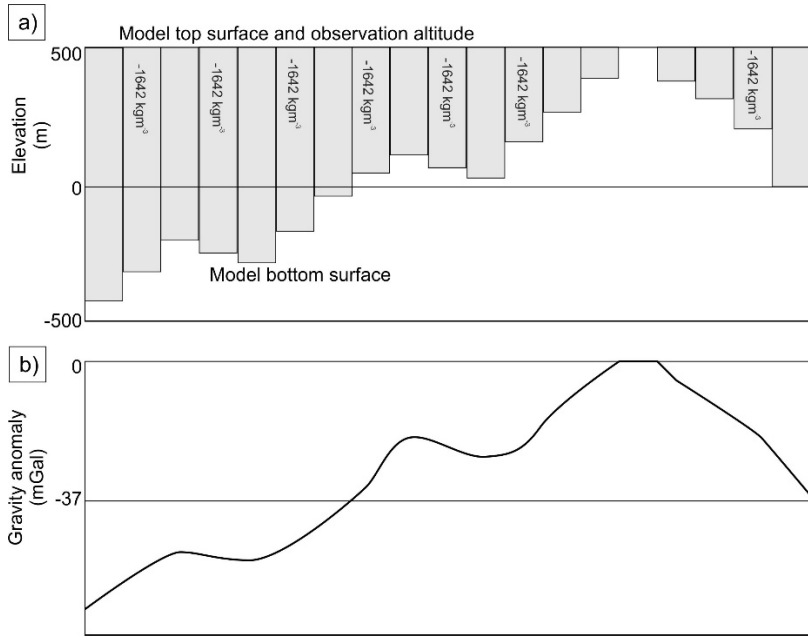
The copyright of individual parts of the supplement might differ from the CC BY 4.0 License.



20 SFig. 1. Range to ice surface for gravity flights used in this compilation (thin black lines). Note most flights cluster around 450 m \pm 200 m above the surface.



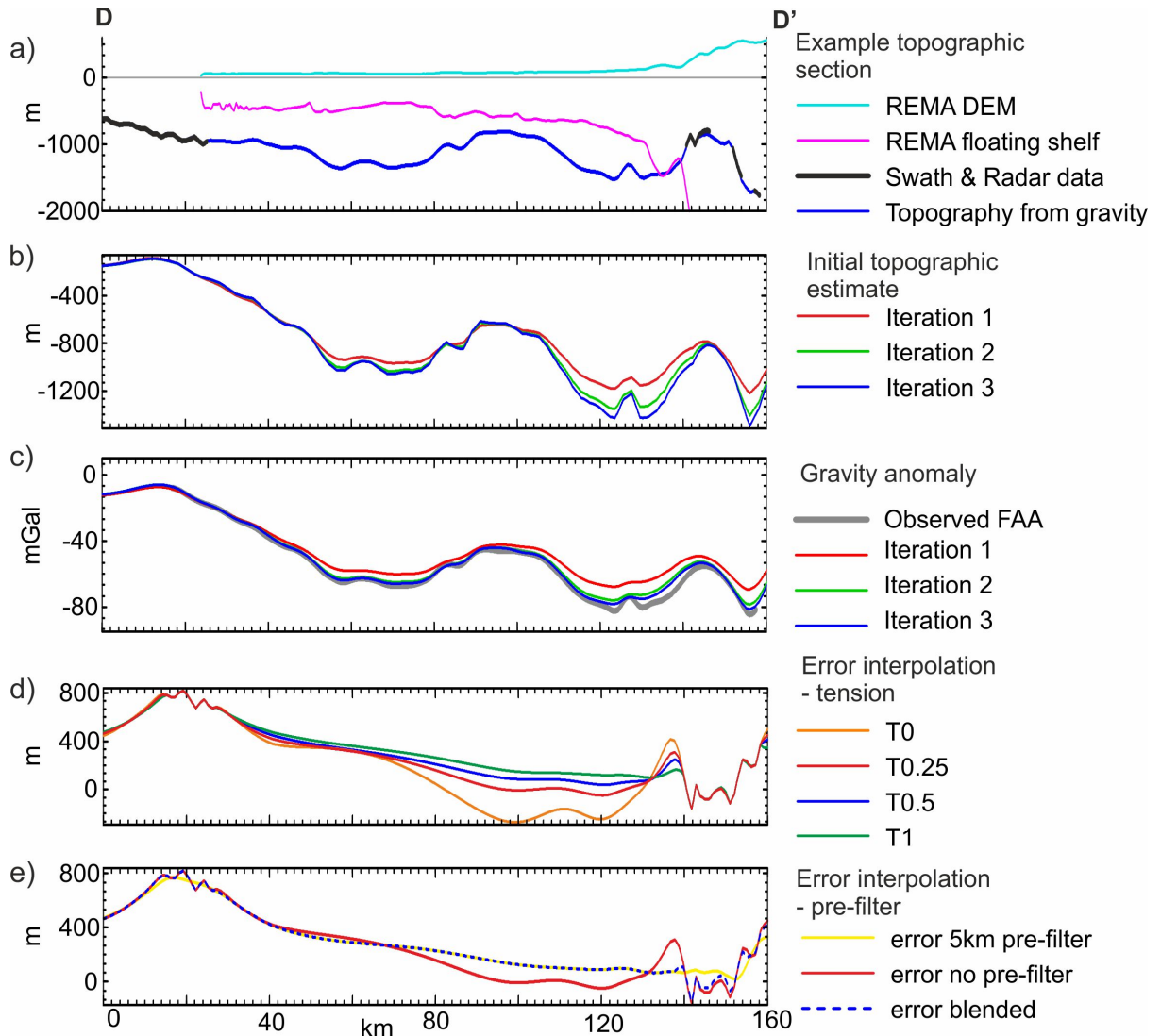
SFig. 2. Intermediate processing stages for recovering bathymetry using the topographic shift method. a) Initial equivalent topography recovered by iterative modelling of free-air gravity anomaly. Edge of free-air data in yellow. Profile D to D' shown in SFig. 4. b) Difference between observed topography (Main text Fig. 1d) and initial equivalent topography in (a) used in calculation of the final bathymetry. Strong colours show differences where both topographic observations and gravity data are present. Pale colours show interpolated difference field. c) Difference field interpolated with a tension of 0.25 and no pre-filter. d) Difference field interpolated with a tension of 0.25 after a 5km pre-filter of observed differences.



30

SFig. 3. Sketch of gravity model setup and output. a) Structure of gravity model. The Gauss–Legendre quadrature (GLQ) method calculates the gravity effect of prisms of material. To efficiently calculate the gravity effect of a bathymetric surface (rock vs water) a series of prisms with this density contrast are therefore considered. b) Sketch of recovered gravity model. Note zero mGal where elevation is +500m.

35



SFig. 4. Example cross section over Dotson Ice Shelf showing intermediate processing stages. See SFig. 2 for location.

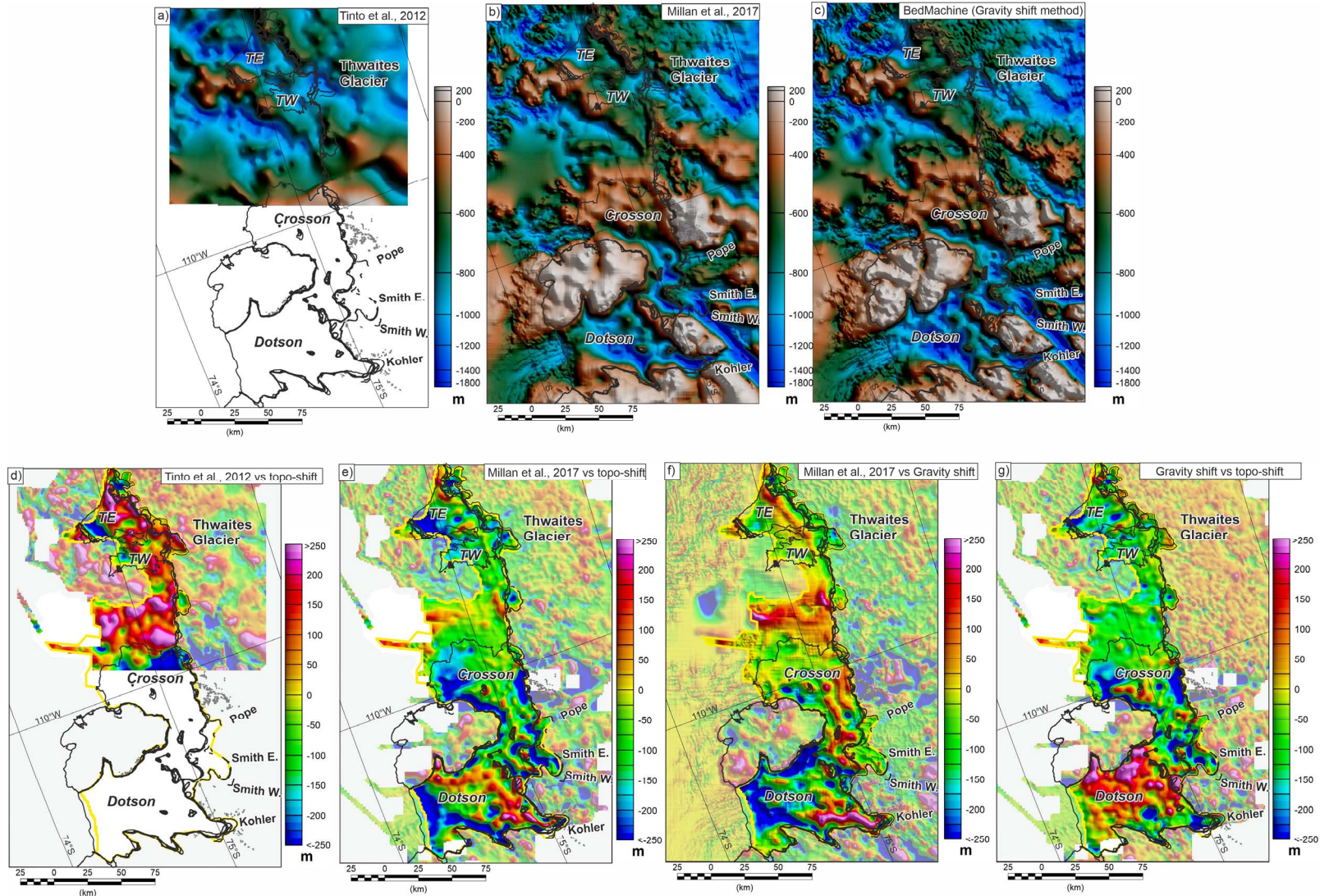
a) Output bathymetry, together with constraining swath and radar elevations.

b) Initial topography during model iterations. Note Iteration 1 is the simple Bouguer slab conversion of the free air gravity anomaly to equivalent topography.

c) Observed and modelled gravity anomalies with mean offset removed. Note rapid convergence along most of the profile.

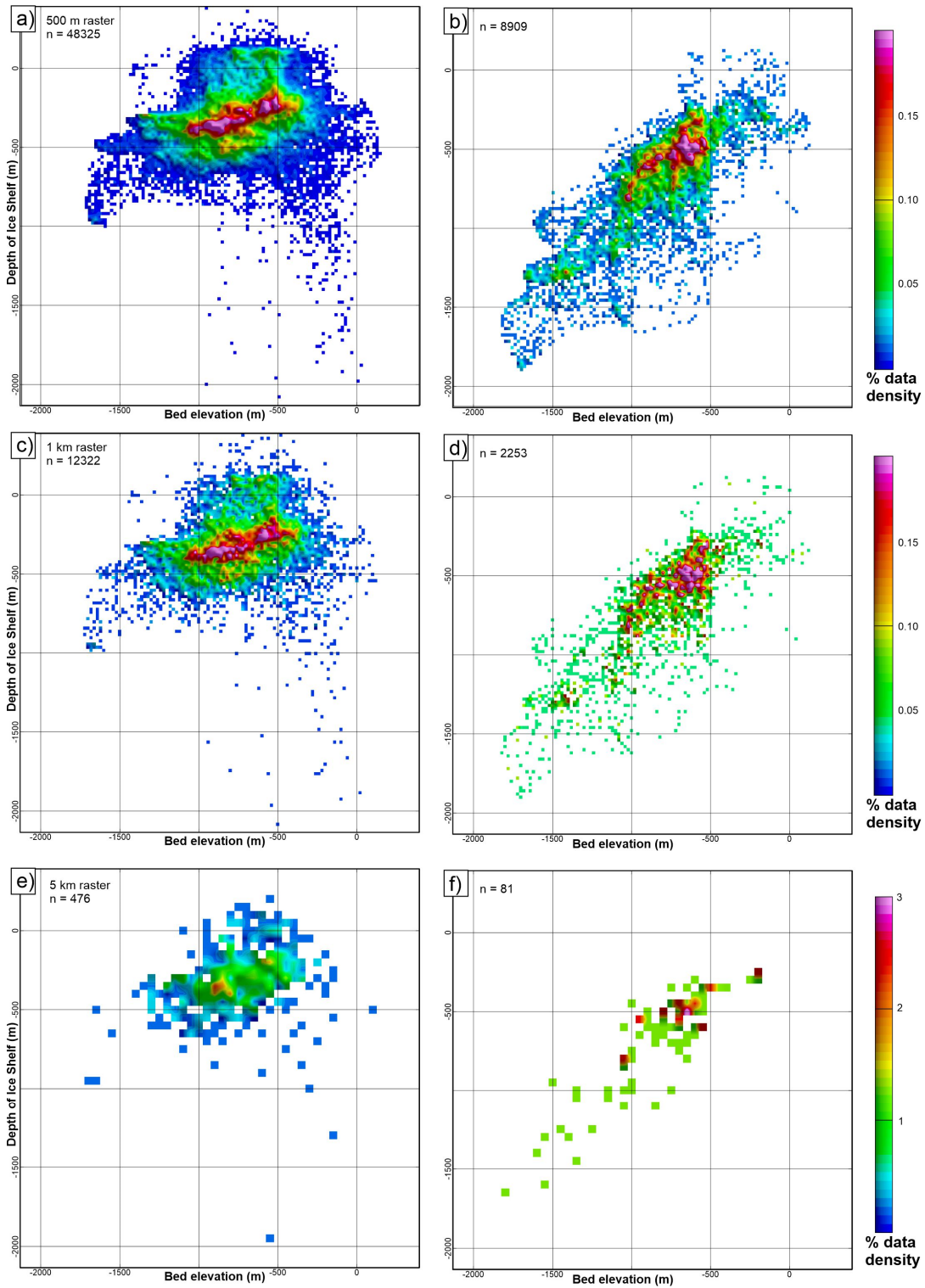
d) Impact of different interpolation tension factors (T_0 to T_1) on the interpolated error field.

e) Impact of 5km pre-filter on interpolation of the error field, and final blended interpolated error field used to correct initial topographic estimate.



45

SFig. 5. Alternative gravity inversion results (a-c) and comparisons (d-g). Note errors in areas where data is constrained by other techniques are grey shaded. Differences in these areas do not reflect the differing gravity inversion methods, and are not discussed in this paper. a) Operation Ice Bridge (OIB) L3 V1 gravity to bathymetry inversion (Tinto et al., 2011). b) Millan et al., 2017 forward modelling result, tied to single coastal offset. c) BedMachine Antarctica (Morlighem et al., 2020) which used the “gravity shift method” (An et al., 2019). d) Comparison of topographic shift method with OIB result. e) Comparison of topographic shift method with Millan et al 2017. f) Comparison between BedMachine gravity shift method and Millan et al., (2017). g) Comparison of topographic shift and BedMachine implementation of the gravity shift method.



SFig. 6. Comparing ice shelf draft at different raster resolutions to new gravity derived sub ice shelf bathymetry. Left hand column is the comparison of the ice shelves in existence prior to 1993. Right hand column is the comparison for ice shelves which developed due to un-grounding after 1993. The n value indicates the number of grid nodes where ice shelf draft and gravity derived bathymetry were co-sampled. a-b 500m ice shelf raster (as in Figure 5. Main text). c-d 1 km ice shelf raster. e-f 5 km ice shelf raster. Note that although the number of grid nodes (n) reduces dramatically, for the ice shelves which developed due to un-grounding after 1993 the ~1:1 correlation between bed elevation and ice shelf depth remains.

Section S1. Calculating sub-ice-shelf bathymetry using the topographic shift method

60 *Step 1 – calculation of the initial bathymetric estimate*

To calculate the sub-ice-shelf bathymetry the topographic shift method first calculates the “initial bathymetric estimate” by converting the free-air gravity anomalies to equivalent variation in topography (SFig. 2a). In the original implementation of the algorithm the Bouguer slab formula was used to directly calculate the initial bathymetric estimate (Hodgson et al., 2019). However, tests using a 3D model of the gravity anomaly associated 65 with a 500 m deep, box shaped trough show that the Bouguer slab technique underestimates the topographic amplitude of narrower features, with errors of up to 10% for a modelled trough 10 km wide. We therefore applied an iterative forward modelling approach to recover a more accurate initial bathymetric estimate. For the gravity modelling we used a Gauss-Legendre Quadrature technique to model the gravity effect of a theoretical bathymetric surface (von Frese et al., 1981). This method calculates the gravity effect of a series of prisms on a 70 1 km x 1 km mesh (SFig. 3). An observation altitude of 500 m was assumed, and a density contrast of -1642 kgm⁻³ was imposed, equivalent to the contrast between water (1028 kgm⁻³) and rock (2670 kgm⁻³). These assumptions are valid as our study focuses on recovering sub-ice-shelf bathymetry, and the larger onshore ice versus rock density contrast is therefore neglected. The effect of the floating ice shelf is ignored as the gravity effect of the surface topography will be balanced by the effect of the low density keel to within the resolution of 75 our data. The model assumptions led to a ~37 mGal mean offset in the calculated gravity field which was removed before comparison with the observed data.

To initiate the gravity inversion (iteration 1), we converted the free-air anomaly to equivalent topography using the Bouguer slab formula (SFig. 4b). The gravity field was modelled (SFig. 4c) and the residual between observed and modelled gravity anomalies were calculated. The bathymetric surface was iteratively adjusted to 80 reduce the calculated residual. An example profile shows how the topography changes with each iteration (SFig. 4b) and the convergence of modelled and observed gravity anomalies (SFig. 4c). It is apparent that the topographic iteration has not totally stabilised, but further iteration would over-fit the gravity data, potentially exaggerating the underlying bathymetry. After two stages of iteration the modelled and observed gravity field had converged to better than +/- 1 mGal across most of the survey area. Topography predicted to be above the 85 observation surface was truncated, and the model did not converge in these regions.

Step 2 – correction to match observed topography

In the second stage, the algorithm corrects for differences between the initial bathymetric estimate (SFig. 2a) and topographic observations (Main text Fig. 1d). The calculated difference between the observed and initial bathymetric estimate reflects an integration of all geological factors, including long wavelength regional 90 variations such as crustal thickness and more local factors such as sedimentary basins or intrusions (SFig. 2b). We assume that the calculated geologically-derived errors vary smoothly away from the constraining points and interpolate the difference field across the study area (SFig. 2b).

Creating and interpolating the difference field (SFig. 2b) is a critical step in calculating the sub-ice-shelf bathymetry. To estimate the difference field away from the control points we used tensioned spline 95 interpolation, as previously suggested for gridding both potential-field and bathymetric data (Smith and Wessel

1990). This technique has two end members, tension (T) = 0, equivalent to a minimum curvature fit to the data, and $T=1$, which provides an approximately linear interpolation between the control points (SFig. 4d). The minimum curvature approach is liable to generate extraneous oscillations away from control points, while a linear interpolation between the control points would be geologically unlikely. We therefore impose a tension factor of 0.25 which produces a result mid-way between the two end members (SFig. 4d).

100 Isolated short wavelength variations in topography at the edge of the control data-set can have a disproportionate impact on the interpolated difference field. This effect is mitigated by calculating the mean difference within a 5 km window before interpolation (SFig. 4e). In regions with control data a difference grid interpolated with no pre-filter was used (SFig. 2c), while away from the control data the interpolated difference 105 grid after the 5 km pre-filter is used (SFig. 2d). The transition between these two regions was blended using a weighted mean varying from zero to one over a 5km Gaussian smoothed transition zone around the observed data.

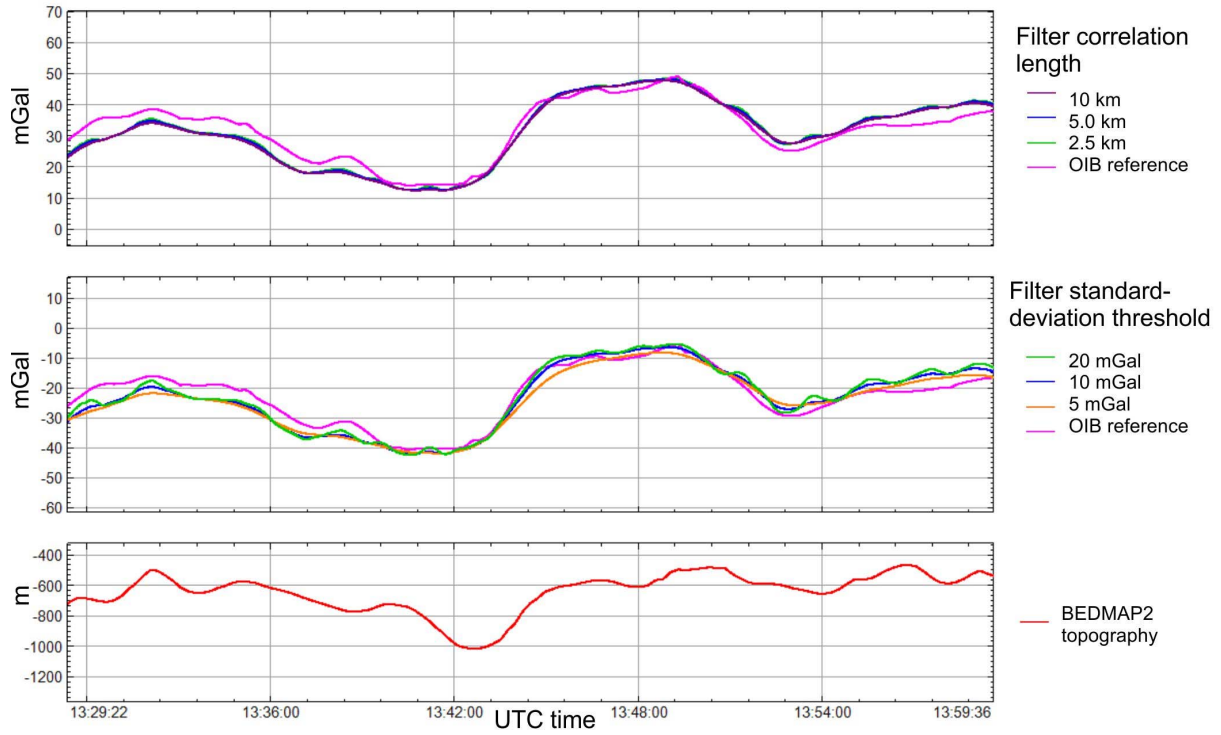
Section S2. International Thwaites Glacier Collaboration (ITGC) airborne gravity data processing.

110 Gravity data during the ITGC survey were collected on the BAS geophysically equipped twin otter using a strapdown gravity system (Jordan and Becker, 2018; Becker et al., 2015; Schwarz and Wei, 1990), and are available from the UK Polar Data Centre (Jordan et al., 2020). Average flight speed was $\sim 60 \text{ ms}^{-1}$, and flights were flown draped, i.e. at an approximately constant terrain clearance, at 450 m. Raw acceleration data were recorded using an iMAR RQH-4001 inertial measurement unit (IMU) owned by Lamont- Doherty Earth 115 Observatory. This sensor package, consists of three Honeywell QA2000 accelerometers (mounted in mutually perpendicular directions), and three ring laser gyroscopes. Coincident GPS data were recorded with a NovAtel receiver.

120 GPS and IMU data were ingested into the Terratec kinematic post processing software TerraPos and solved for a tightly coupled positional solution using a Precise Point Positioning (PPP) method. This included using precise ephemeris downloaded three months after data collection. The GPS antenna/INS lever arm was solved iteratively through three iterations of TerraPos and converged on: $x=0.1881$ $y=0.3734$ $z=-1.5072$ with variations at a sub cm level. Once the lever arm had been established this value was used for all subsequent flights, and the free-air gravity anomaly from the GRS80 ellipsoid was calculated at the same time as the position. Position, attitude and gravity data were then exported as 1Hz ASCII files which were imported into Geosoft Oasis 125 Montage software suite for further analysis and levelling of the gravity data.

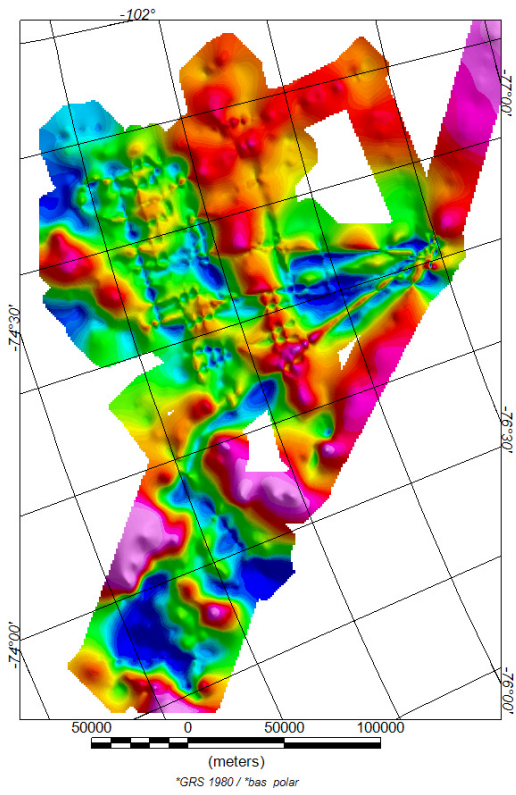
During the initial gravity processing Kalman filter parameters associated with the output gravity values were a 5km gravity correlation constant and a 10 mGal standard deviation. The stated performance of the iMAR IMU was also included in the Kalman filter. The correlation and standard deviation values were the system defaults in the TerraPos software and were used for all processing. Parameter tests of the impact of correlation and standard 130 deviation were carried out and compared to Operation ICEBRIDGE (OIB) data (SFig. 7). These comparisons suggest the correlation factor has limited impact, but that it could in future be reduced to 2.5km. Increasing the

permitted standard deviation to 20 mGal gives a relatively noisy signal, while reducing the permitted standard deviation to 5 mGal gives an overly smooth solution.



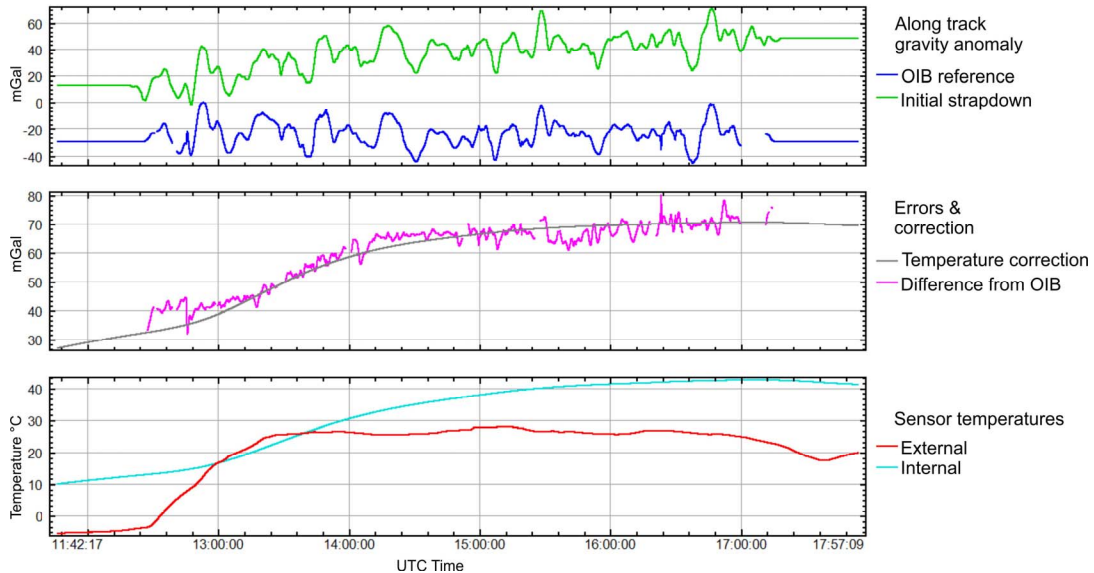
135 SFig. 7. Impact of assumed correlation distance (top panel) and allowed gravity standard deviation (middle panel) on recovered free-air gravity values. For comparison OIB data gravity data collected on a coincident line are shown. Gravity outputs are not temperature corrected, but are all shown with the same amplitude vertical scale. Note the OIB data is sampled from a grid so artefacts due to cross lines may be present. Lower panel shows bed topography from BEDMAP2.

140 Overall the free air anomalies after initial processing show a clear geological/bathymetric pattern and correspond at short wavelengths to OIB data, but significant line to line noise is apparent (SFig. 8 and 9). To quantify this noise we compare our output free-air anomaly with gridded data from the OIB campaign in this region (SFig. 9). There is a clear pattern across every flight with a shift of ~30mGal at the start of each flight, and a shift of ~60 mGal at the end.



145

SFig. 8. Map of initial free-air gravity anomalies prior to thermal correction.

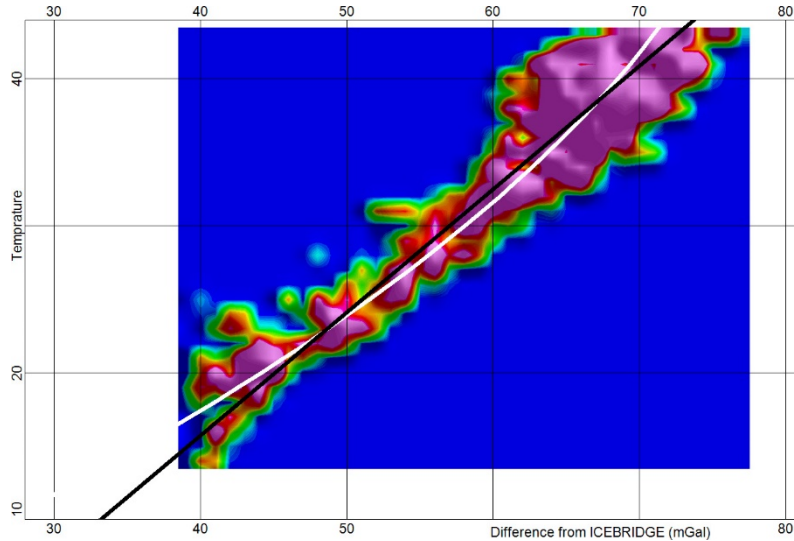


SFig. 9. Example of initial processed free-air gravity anomaly along an entire flight, together with reference OIB data, and thermal effects and correction.

150 Plotting the internal sensor temperature reported for the IMU against the difference with OIB data confirmed that this error is dominantly a temperature effect (SFig. 10). Generally the errors for all flights cluster along one path, but one flight has a systematic additional shift. The errors for this anomalous flight, together with errors far from the main cluster were discarded to get a better view of the temperature-induced error curve (SFig. 9).

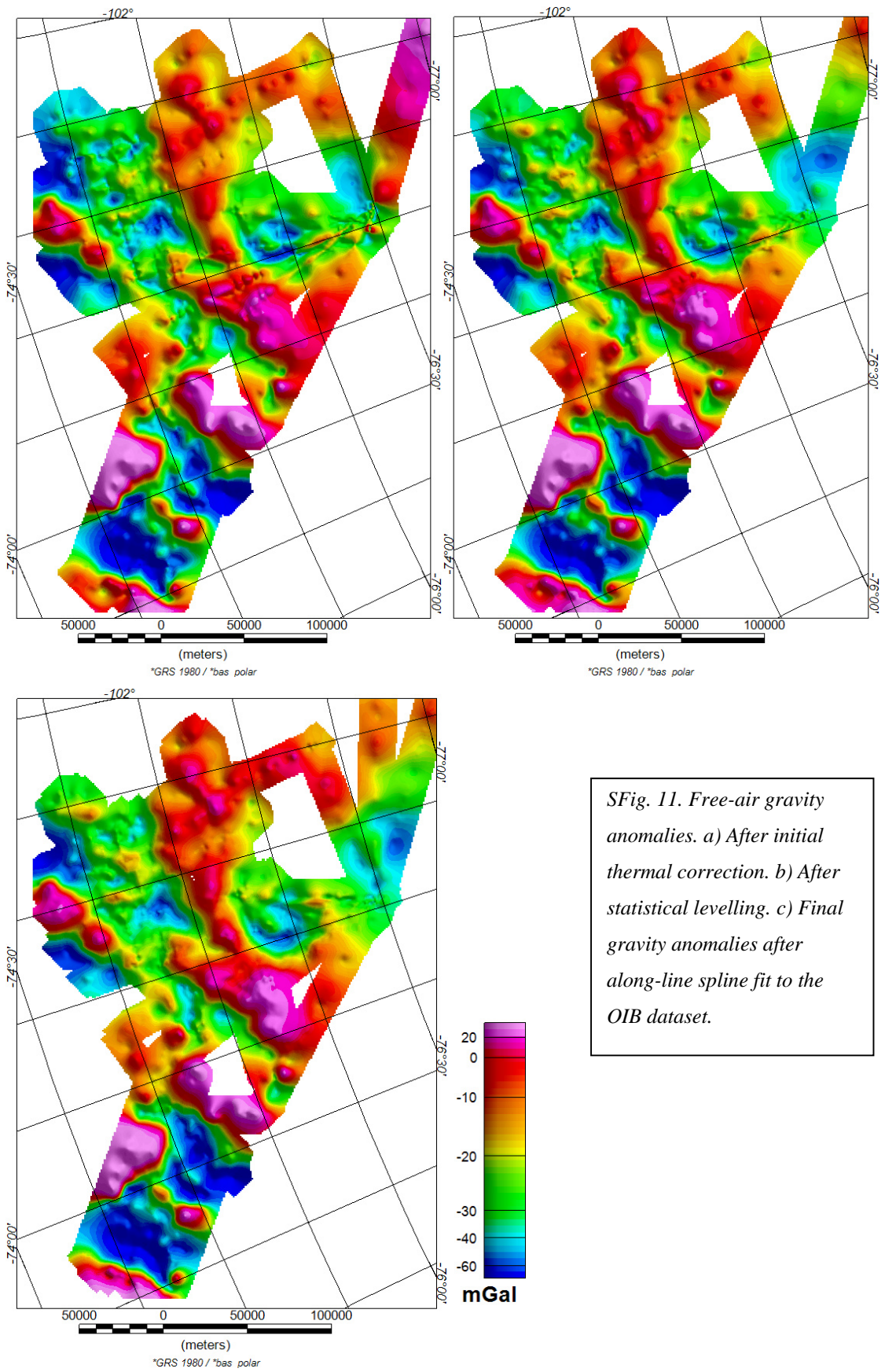
Taking these edited data points into Microsoft Excel and fitting a 2nd order polynomial provided our model for
155 the thermal drift:

$$\text{Thermal error mGal} = -0.0174T^2 + 2.2619T + 5.8554$$



SFig. 10. Temperature vs difference with OIB data density plot. Pink indicates many data points, blue indicates no data points. Note the data cluster is approximated by a straight line, with slope of $1.1934T$ (black). However,
160 the 2nd order polynomial (white) tracks the error field more precisely.

After correcting for the overall thermal effects (SFig. 11a) the crossover error was 7.09 mGal. Subsequent simple statistical levelling using a 3rd order trend fit to the crossover errors along each flight reduced the error to 2.84 mGal (SFig. 11b). At this stage small residual errors with OIB on the order of +/- 3 mGal, with a wavelength of ~340 km (~2 hours) were evident. To remove this final error extreme errors, greater than +/-
165 8mGal, assumed to be gridding artefacts, were removed from the error values. A B-spline with smoothness of 1 and tension of zero (minimum curvature) was then fit to the residual error, and the resulting trend subtracted from the levelled free air anomaly. The final standard deviation of the crossover errors is 2.2 mGal, which equates to an error of 1.56 mGal (SFig. 11c).



SFig. 11. Free-air gravity anomalies. a) After initial thermal correction. b) After statistical levelling. c) Final gravity anomalies after along-line spline fit to the OIB dataset.

References

- An, L., Rignot, E., Millan, R., Tinto, K., and Willis, J.: Bathymetry of Northwest Greenland Using
175 "Ocean Melting Greenland" (OMG) High-Resolution Airborne Gravity and Other Data,
Remote Sensing, 11, <https://doi.org/10.3390/rs11020131> 2019.
- Becker, D., Nielsen, J. E., Ayres-Sampaio, D., Forsberg, R., Becker, M., and Bastos, L.: Drift reduction
in strapdown airborne gravimetry using a simple thermal correction, Journal of Geodesy, 89,
1133-1144, 2015.
- Hodgson, D. A., Jordan, T. A., De Rydt, J., Fretwell, P. T., Seddon, S. A., Becker, D., Hogan, K. A., Smith,
180 A. M., and Vaughan, D. G.: Past and future dynamics of the Brunt Ice Shelf from seabed
bathymetry and ice shelf geometry, The Cryosphere, 13, 545-556, 10.5194/tc-13-545-2019,
2019.
- Jordan, T. A., and Becker, D.: Investigating the distribution of magmatism at the onset of Gondwana
185 breakup with novel strapdown gravity and aeromagnetic data, Physics of the Earth and
Planetary Interiors, 282, 77-88, <https://doi.org/10.1016/j.pepi.2018.1007.1007>, 2018.
- Jordan, T. A., Robinson, C., Porter, D., Locke, C., and Tinto, K.: Processed line aerogravity data over
the Thwaites Glacier region (2018/19 season). Natural Environment Research Council, UK
Research & Innovation, UK Polar Data Centre, 2020.
- Morlighem, M., Rignot, E., Binder, T., Blankenship, D., Drews, R., Eagles, G., Eisen, O., Ferraccioli, F.,
190 Forsberg, R., Fretwell, P., Goel, V., Greenbaum, J. S., Gudmundsson, H., Guo, J., Helm, V.,
Hofstede, C., Howat, I., Humbert, A., Jokat, W., Karlsson, N. B., Lee, W. S., Matsuoka, K.,
Millan, R., Mouginot, J., Paden, J., Pattyn, F., Roberts, J., Rosier, S., Ruppel, A., Seroussi, H.,
Smith, E. C., Steinhage, D., Sun, B., Broeke, M. R. v. d., Ommen, T. D. v., Wessem, M. v., and
Young, D. A.: Deep glacial troughs and stabilizing ridges unveiled beneath the margins of the
195 Antarctic ice sheet, Nature Geoscience, 13, 132-137, 10.1038/s41561-019-0510-8, 2020.
- Schwarz, K. P., and Wei, M.: A framework for modelling kinematic measurements in gravity field
applications, Journal of Geodesy, 64, 331-346, 10.1007/BF02538407, 1990.
- Tinto, K., Bell, R. E., and Cochran, J. R.: IceBridge Sander AIRGrav L3 Bathymetry, Version 1., NASA
200 National Snow and Ice Data Center Distributed Active Archive Center., Boulder, Colorado
USA., 2011.
- von Frese, R. R. B., Hinze, W. J., Braile, L. W., and Luca, A. J.: Spherical earth gravity and magnetic
anomaly modeling by Gauss- Legendre quadrature integration, Journal of Geophysics, 49,
234-242, 1981.

205